[17] Implementation of an algorithm for forming a color image from monochrome images of visible and near infrared cameras in the YCbCr color space

I.S. Kholopov [1,2]
[1] *Ryazan State Radio Engineering University, Ryazan, Russia,*
[2] *Joint Stock Company Ryazan State Instrument-making Enterprise, Ryazan, Russia*

Abstract

We consider a simplified algorithm for fusion of greyscale visible and thermal images presented in false colors in the de-correlated YCbCr color space. The color gamut is then brought to daylight conditions using a color transfer algorithm that provides the same luminosity of the resulting gray fusion and color fusion images. It is shown that the parallel computing on the graphics card performs real-time video fusion with a frame size of up to 1024×768 pixels and a frame rate of 30 Hz.

Keywords: *RGB, HSI, YUV and YCbCr color spaces, infrared image, image fusion, false color, color transfer algorithm, histogram, and bilinear interpolation.*

Citation: *Kholopov IS. Implementation of an algorithm for forming a color image from monochrome images of visible and near infrared cameras in the YCbCr color space. Computer Optics 2016; 40(2): 266-274. DOI: 10.18287/2412-6179-2016-40-2-266-274.*

Introduction

A new class of electro-optical systems known as *Enhanced Vision Systems* (EVS) has been developed to observe subjects in adverse conditions (smoke, dust, fog, rainfall, background illumination, low light conditions, masking, etc.). By the 'enhanced vision' we should basically mean [1] a set of transformations aimed at enhancing a contrast and emphasizing an image skeleton that contribute most to the selection of subjects in perceived images. The development of EVS usually involves, apart from the use of television (TV) sensors for visible wave ranges (380–760 nm), also the use of thermal imaging (TI) sensors in the *Short Wave Infrared* (SWIR) range (wavelength from 0.9 to 1.7 microns), *Medium Wave Infrared* (MWIR) range (wavelength from 3 to 5 microns) or *Long Wave Infrared* (LWIR) range (wavelength from 8 to 14 microns) in channels of *Computer Vision Systems* (CVS). Data integration in multispectral monochrome sensors is implemented using image fusion algorithms. In this case, the resulting images have greater informative value than particular images from each channel of the multispectral CVS [1–5]. If all sensors of the CVS form grayscale images, the informative value of the resulting fusion image can be additionally increased by presenting it in *false colors*. The color gamut is then brought to natural colors (*true colors*) [6–10].

The purpose of this paper is to implement a simplified algorithm for forming color fusion images from grayscale images in TV and TI *Long Wave Infrared* ranges.

1. Research objective

It is expected that the research objective discussed in this paper, referring to color fusion image framing based on grayscale images from TV and TI sensors, shall be solved by means of the following procedures to be acted upon:

- alignment between fields of view in TV and TI cameras;
- grayscale fusion to form a brightness (achromatic) component of the resulting image;

- proper color fusion imagery for forming chromatic components.

Each of the above first two procedures may present a separate research subject, therefore, the main approaches to solving this task is synopsized below.

Vision alignment algorithms for multispectral sensors

The main reasons for mismatching frame elements in video sensors of the multichannel CVS, according to paper [11], are as follows:

- the difference between mutual positions of cameras and subjects;
- different matrix resolutions in CVS cameras;
- different lens fields of view and their distortion;
- the lack of frame exposure timing synchronization (when moving objects observed).

Video sensors of the multispectral CVS (cameras K1 and K2 in Fig. 1) can use both a shared optical channel with a Beam Splitter (BS) (Fig. 1*a*), dividing waves of visible and infrared ranges, and separate optical channels (Fig. 1*b*). In the first case, the additional use of mechanical alignment would allow us to roughly combine apparent optical centers of the sensors and thus to minimize projective distortions.

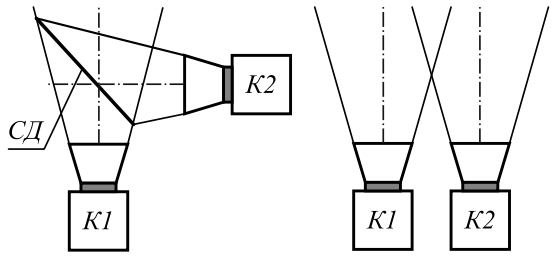

a) *b)*

Fig. 1. Matching (a) and overlapping (b) fields of view in sensors of the two-camera CVS in different arrangements

In the second case, the effect of noncollinearity of optical axes of the cameras and diversity of their optical centers should result in projective distortions and the effect of optical parallax. However, precisely this approach (due to smaller dimensions of a camera system) is the most often practiced.

The problem of alignment of the *i*-th and *j*-th images taken from spaced cameras in the same spectral range (subject to the correction of distortion of their lenses) is successfully solved by using the following matrix transformation:

$$\mathbf{x}_i = \mathbf{H}_{ij}\mathbf{x}_j,$$

where $\mathbf{H}_{ij}$ is a homography matrix connecting homogeneous pixel coordinates of images of the *i*-th and *j*-th cameras $\mathbf{x}_i = [u_i, v_i, 1]^{\mathrm{T}}$ and $\mathbf{x}_j = [u_j, v_j, 1]^{\mathrm{T}}$, respectively; (u, v) are the coordinates of a pixel located over the intersection of the u-th line and the v-th column. Since the coordinates of $\mathbf{x}_i$ are fractional, the bilinear interpolation is used to identify the pixel brightness in nodes of a coordinate grid [12].

Evaluation of the homography matrix is usually based on the selection of pairs of corresponding image points and description of their neighborhoods by means of various descriptors [13]. The main constraint on application of algorithms for automatic search of proper pairs for matching the images from two multispectral cameras is the difference in the brightness of image subjects in different ranges (visible, MWIR, and LWIR). In this regard, based on the analysis presented in [11, 14-22], it is possible to identify four basic approaches to alignment of different fields of view in spaced multispectral sensors.

1. Brightness correlation alignment using image pyramids [14].
2. Correlation alignment based on results of profile analysis [15–17].
3. Alignment through evaluating the homography matrix by matching special points. For this purpose, the authors of papers [18, 19] note that to evaluate the homography matrix, some image interrelationships with different spectral ranges are determined manually.
4. Preliminary camera calibration by flat chess pattern [20–22].

As justly noted in paper [23], the latest approach is not applicable in imaging by only one moving camera. However, for multispectral CVS, where video sensors are fixed on a hard base and don't change their positions relative to each other in the course of imaging, this approach is the most robust in observing low-contrast subjects and/or in low-light conditions when the efficiency of approaches 1-3 has been going downward [24].

By reason of the above noted feature (the difference in the brightness of image subjects from cameras with different ranges), for the purpose of calibration (evaluation of matrices of camera internal parameters $\mathbf{K}_i$ and $\mathbf{K}_j$, rotation matrix $\mathbf{R}_{ij}$, and translation vector $\mathbf{t}_{ij}$), we would recommend to use a flat noncombustible pattern that is a combination of patterns from papers [20] and [22] (Fig. 2).

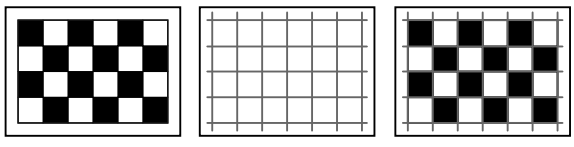

a) *b)* *c)*

Fig. 2. Calibration patterns: a chess-type pattern for TV cameras (a); a pattern with driven filaments for TI cameras in the MWIR or LWIR ranges (b); a combined-type pattern for calibration of TV and TI cameras (c)

Since the relationship between the homography matrix and camera calibration parameters i and j is determined by formula [25]

$$\mathbf{H}_{ij} = \mathbf{K}_i(\mathbf{R}_{ij} - \mathbf{t}_{ij}\mathbf{n}^{\mathrm{T}}/d)\mathbf{K}_j^{-1},$$

where $\mathbf{n}$ and d are a normal vector to imaging plane and its linear distance in the coordinate system of the j-th camera, respectively, the following approximate equation holds true for the subjects observed, where the distance d is much more than the linear distance between the cameras $||\mathbf{t}_{ij}||$ and where $||\times||$ are two vector norms:

$$\mathbf{H}_{ij} \approx \mathbf{K}_i\mathbf{R}_{ij}\mathbf{K}_j^{-1}.$$

In this paper, when analyzing color-based image fusion algorithms, we used images and videos (30 fps) with already combined fields of view in TV and TI sensors.

Grayscale and multispectral image fusion algorithms

The resulting grayscale image fusion algorithm may be generally written in the form of the following functional:

$$Y_F(i,j) = F\{TV(i,j), TI(i,j)\}, \quad (1)$$

where $TV(i,j)$ and $TI(i,j)$ are the pixel brightness for TV and TI images over the intersection of the i-th line and j-th column, and $Y_F(i,j)$ is the pixel brightness after fusion.

The most simple, and therefore, computationally less capacious image fusion algorithms for two spectral ranges (TV and TI) forming high-contrast halftone images are as follows:

- the equilibrium algorithm (arithmetic mean algorithm) [3],
- $Y_F(i,j) = [TV(i,j) + TI(i,j)]/2;$ (2)
- the fusion TV channel algorithm [1, 26],
- $Y_F(i,j) = TV(i,j) + |TI(i,j) - \overline{TI}| - \Delta TI$, (3)
- where $\Delta TI = |TI(i,j) - \overline{TI}|$;
- the image fusion algorithm based on contrast pyramids (Laplacian and Gaussian) or wavelet transforms [2, 4];
- the spatial frequency fusion algorithm using mathematical methods of discritization and resynchronization of multivariable messages and a 3D (two 3D coordinates and one spectral coordinate) low-pass interpolation filter [27].
- In this paper, we used algorithm (2) for grayscale fused imaging followed by the histogram reduction method [28, 29].

2. Comparative analysis of IR ranges

The use of the SWIR, MWIR and LWIR ranges is caused by the presence of atmospheric transparency windows at the given wavelengths λ [30–32], where the transmission factor of infrared radiation η exceeds a value of 0.5 (Fig. 3).

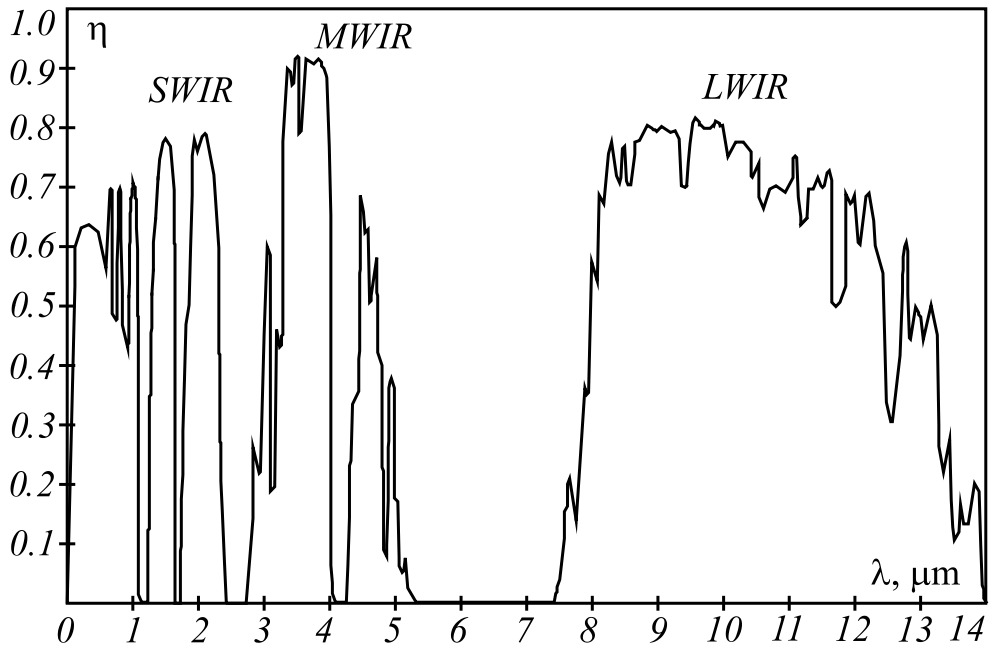

Fig. 3. Atmospheric transparency windows

Based on the advantages and disadvantages [30,31] for each of the infrared ranges given below in Table 1, the MWIR or LWIR sensors are usually used in EVS with a single TI channel.

Table 1. Comparative analysis of IR ranges

IR range	Advantages	Disadvantages
SWIR	- similarity of SWIR images with images of visible range: a sensor records subject-reflected light rather than its thermal infrared radiation; - larger visual range, versus visible range, of subjects in adverse conditions (rainfall, smoke, dust, fog, etc.); - twice larger value of natural night light versus visible range;	- low video quality at light intensity of less than 0.2 lx; - different column extension in matrix sensors assembled from SWIR sensor rulers;
MWIR	- better contrast of sky-and-earth imagery; - the least attenuation during propagation in the atmosphere;	- excessive contrast for strongly heated and burning objects compared to LWIR;
LWIR	- better visibility in smoke/dust conditions and at low temperatures compared to MWIR; - not subject to the effect of sunglint.	- lager atmospheric attenuation compared to MWIR.

3.False color enhancement algorithms. Color transfer

The idea to form color images from grayscale TV and TI imagery is based on application of the following functionals:

$R_f(i,j) = f_R\{TV(i,j), TI(i,j)\}$,
$G_f(i,j) = f_G\{TV(i,j), TI(i,j)\}$,
$B_f(i,j) = f_B\{TV(i,j), TI(i,j)\}$,

where $R_f(i,j)$, $G_f(i,j)$, $B_f(i,j)$ are the *RGB*-components of pixels in an image; index *f* denotes a false color image. Usually [6–9], a TI component is fed to *R*-channel, whereas a TV component – to *G*-channel:

$$\begin{aligned} R_f(i,j) &= TI(i,j),\\ G_f(i,j) &= TV(i,j),\\ B_f(i,j) &= TV(i,j) - TI(i,j), \end{aligned} \tag{4}$$

or

$$\begin{aligned} R_f(i,j) &= TI(i,j),\\ G_f(i,j) &= TV(i,j),\\ B_f(i,j) &= TV(i,j). \end{aligned} \tag{5}$$

A somewhat different solution was proposed in [10]:

$$\begin{aligned} R_f(i,j) &= [TV(i,j) + TI(i,j)]/2,\\ G_f(i,j) &= TI(i,j),\\ B_f(i,j) &= TV(i,j) - TI(i,j). \end{aligned} \tag{6}$$

The false color images obtained according to (4)–(6) are difficult for perception, since they have unnatural colors of the sky and plants [7, 9].

Paper [33] shows that in de-correlated color space Lαβ a color gamut may be transferred from a target image by replacing the mathematical expectation and the root-mean-square deviation (RMSD) of chromatic components as follows:

$$\theta(i,j) = [\theta(i,j)_s - \mu_s^\theta]\sigma_t^\theta/\sigma_s^\theta + \mu_t^\theta, \tag{7}$$

where $\theta(i,j) = \{\alpha(i,j), \beta(i,j)\}$, index *s* and index *t* mean, respectively, a *source* image and a *target*, whereas symbols μ^θ and σ^θ denote, respectively, the mathematical expectation and RMSD of parameter θ being estimated by picture frame.

It is desirable to select the target in such a way that its color gamut would approximately correspond (with regard to the type of locality and phonological conditions) to the color gamut of the observed scene [34]. To reduce computing costs on estimation of parameters μ_t^θ and σ_t^θ in paper [35], it is proposed to display target images as the 1st and 2nd order central moment vectors $\mathbf{V}_t = ||\mu_t^{\theta_1}, \mu_t^{\theta_2}, \sigma_t^{\theta_1}, \sigma_t^{\theta_2}||^T$, where θ_1 and θ_2 are multicolor channels, which may be stored in a target bank and selected, for example, according to data obtained from geographic information and satellite radio navigation systems.

For computational simplicity in transferring the *RGB* color space into the de-correlated color space and vice versa, in paper [6, 8] it is proposed to use other de-correlated spaces, i.e. *YUV* and YC_bC_r:

$$\begin{bmatrix} Y \\ U \\ V \end{bmatrix} = \begin{bmatrix} 0.2990 & 0.5870 & 0.1140 \\ -0.1471 & -0.2888 & 0.4359 \\ 0.6148 & -0.5148 & -0.1 \end{bmatrix} \begin{bmatrix} R \\ G \\ B \end{bmatrix},$$

$$\begin{bmatrix} Y \\ C_b \\ C_r \end{bmatrix} = \begin{bmatrix} 0.2990 & 0.5870 & 0.1140 \\ -0.1687 & -0.3313 & 0.5000 \\ 0.5000 & -0.4187 & -0.0813 \end{bmatrix} \begin{bmatrix} R \\ G \\ B \end{bmatrix}, \tag{8}$$

with the following inverse transforms:

$$\begin{bmatrix} R \\ G \\ B \end{bmatrix} = \begin{bmatrix} 1.0000 & 0.0000 & 1.4020 \\ 1.0000 & -0.3947 & -0.5808 \\ 1.0000 & 2.0325 & 0.0000 \end{bmatrix} \begin{bmatrix} Y \\ U \\ V \end{bmatrix},$$

$$\begin{bmatrix} R \\ G \\ B \end{bmatrix} = \begin{bmatrix} 1.0000 & 0.0000 & 1.4020 \\ 1.0000 & -0.3441 & -0.7141 \\ 1.0000 & 1.7720 & 0.0000 \end{bmatrix} \begin{bmatrix} Y \\ C_b \\ C_r \end{bmatrix}. \tag{9}$$

The resulting images after color transfer according to (7), if used in the *YUV* and YC_bC_r color spaces, where $\theta(i, j) = \{C_b(i, j), C_r(i, j)\}$, as noted in [6], are nearly identical. The advantage of the YC_bC_r color space, versus the *YUV* color space, is the simplification of calculations of multicolor components, since multiplication by a factor of 0.5 in fixed-point operations is equivalent to arithmetic right shift by 1.

For further simplification of conversion *RGB* -> YC_b-C_r, we may approximately consider that (4) is equivalent to that one given in [34]

$$\begin{aligned} C_{bf}(i,j) &= -TI(i,j)/2, \\ C_{rf}(i,j) &= \left[TI(i,j) - TV(i,j)\right]/2, \end{aligned} \quad (10)$$

(5) –
$$\begin{aligned} C_{bf}(i,j) &= [TV(i,j) - TI(i,j)]/4, \\ C_{rf}(i,j) &= [TI(i,j) - TV(i,j)]/2, \end{aligned} \quad (11)$$

a (6) –
$$\begin{aligned} C_{bf}(i,j) &= TV(i,j)/2 - TI(i,j), \\ C_{rf}(i,j) &= [TV(i,j) - TI(i,j)/2]/4. \end{aligned} \quad (12)$$

In hardware implementation in microprocessors or programmable logic devices, as well as when using fixed-point computing arithmetic, the division operations of halving and quartering shown in (10) – (12) shall be replaced by the quickest operations of arithmetic right shift by 1 and 2, respectively.

It is reasonable to form achromatic component Y_F of the resulting image in color transfer [6 – 8, 34, 36] as the resulting grayscale TV and TI brightness fusion images (1).

4. Options of performance improvement of the color-transfer-based method

Despite the fact that the simplified algorithms for forming multicolor components (10) – (12) allow us to increase the performance of the color-transfer-based algorithm (7) up to 1.8 times [34], compared to calculating multicolor components C_{bf} and C_{rf} according to (4) – (6) and (8), they do not allow us (without applying the parallel computing procedure) to implement the grayscale TV and TI fusion images in full color for video sequences with a frame frequency of over 25 Hz and a frame size of over 640×480 pixels.

To further improve the performance, it is assumed in paper [36] that

$$\begin{aligned} C_{rf}(i,j) &= \left[TI(i,j) - TV(i,j)\right]/2, \\ C_{bf}(i,j) &= -C_{rf}(i,j), \end{aligned} \quad (13)$$

and, therefore,

$\mu^{Cb} = -\mu^{Cr}$, $\sigma^{Cb} = \sigma^{Cr}$,

that allows us to reduce twice the amount of calculations when estimating μ^θ and σ^θ ($\theta = C_b, C_r$).

Further simplification of calculations may involve, similar to [37], replacing the estimated mean square deviation

$$\hat{\sigma}^\theta = \overline{\left(\theta - \mu^\theta\right)^2}^{1/2} \quad (14)$$

by the estimated mean absolute deviation

$$\hat{\sigma}^\theta \approx 5\overline{\left|\theta - \mu^\theta\right|}/4. \quad (15)$$

Indeed, if a centered value $(\theta - \mu^\theta)$ is distributed according to a normal law of zero mathematical expectation

$$w(\theta) = \frac{1}{\sqrt{2\pi}\sigma}\exp\left\{-\frac{\theta^2}{2\sigma^2}\right\},$$

this magnitude will get a law of distribution then

$$w_{\text{mod}}(\theta) = \begin{cases} \dfrac{2}{\sqrt{2\pi}\sigma}\exp\left\{-\dfrac{\theta^2}{2\sigma^2}\right\}, \theta \ge 0, \\ 0, \theta < 0, \end{cases}$$

whereas the mathematical expectation $|\theta - \mu^\theta|$ is equal to the following:

$$\overline{\left|\theta - \mu^\theta\right|} = \int_{-\infty}^{\infty} \theta w_{\text{mod}}(\theta)\,d\theta =$$

$$= \frac{2}{\sqrt{2\pi}\sigma}\int_0^{\infty} \theta\exp\left\{-\frac{\theta^2}{2\sigma^2}\right\}d\theta = 0,798\sigma \approx 4\sigma/5.$$

The main disadvantage of color-transfer-based algorithms is the reduction of luminosity of subjects $I(i, j)$ [35], corresponding to the intensity (brightness of a grayscale image) in achromatic case, by the inverse transformation YC_bC_r -> *RGB* that leads to the necessity of application of color model *HSI* [28]:

$R_n = R/255$, $G_n = G/255$, $B_n = B/255$,

$I = 0.5[\max\{R_n, G_n, B_n\} + \min\{R_n, G_n, B_n\}]$,

$$S = \begin{cases} \dfrac{\max\{R_n, G_n, B_n\} - \min\{R_n, G_n, B_n\}}{\max\{R_n, G_n, B_n\} + \min\{R_n, G_n, B_n\}}, I < 0,5, \\ \dfrac{\max\{R_n, G_n, B_n\} - \min\{R_n, G_n, B_n\}}{4 - \left[\max\{R_n, G_n, B_n\} + \min\{R_n, G_n, B_n\}\right]}, I \ge 0,5, \end{cases}$$

$$H = \begin{cases} 60(G_n - B_n)/S, \max\{R_n, G_n, B_n\} = R_n, \\ 120 + 60(B_n - R_n)/S, \max\{R_n, G_n, B_n\} = G_n, \\ 240 + 60(R_n - G_n)/S, \max\{R_n, G_n, B_n\} = B_n, \end{cases}$$

$$H = \begin{cases} H, H \ge 0, \\ H + 360, H < 0. \end{cases}$$

After color transfer in space *HSI*, the following substitution shall be performed:

$$I(i, j) = Y_F(i, j), \quad (16)$$

The result is that by the inverse transformation *HSI* -> *RGB*, the same luminosity is provided both for

grayscale and color fusion images. A price for equal luminosity is the decrease of a fusion rate by 35 % [35].

5. Experimental results

The purpose of the experiment was to evaluate the performance of image fusion algorithms for TV and TI images followed by the resulting color gamut, most closely approximate to real lighting conditions during their implementation on PCs. The size of TV frames was 1024×768 pixels and TI frames – 512×384 pixels. In our experiment, we used a PC with Intel Core-*i5* processor type with a memory clock rate of 2.8 GHz and the amount of RAM of 4 GB.

In order to evaluate the performance of TV (Fig. 4*a*, *b*) and TI images in the LWIR range (Fig. 4*c*, *d*), the following image fusion algorithms were performed (conventionally, algorithms 1, 2 and 3):

- Algorithm 1 (non-simplified) – evaluation of the *RGB*-components according to (4), transfer to the YC_bC_r color space according to (8), evaluation of standard deviations of the C_{bf} and C_{rf} components in false colors according to (14), color transfer according to (7), changing back to color mode (*RGB)* according to (9), luminosity compensation according to (16);
- Algorithm 2 (simplified algorithm for evaluation of multicolor components [36]) – evaluation of the C_{bf} and C_{rf} components in false colors according to (13) and their standard deviations according to (14), color transfer according to (7), changing back to color mode (*RGB)* according to (9), luminosity compensation according to (16);
- Algorithm 3 (simplified algorithm for evaluation of multicolor components and their standard deviations) – evaluation of the C_{bf} and C_{rf} components in false colors according to (13) and their standard deviations according to (15), color transfer according to (7), changing back to color mode (*RGB)* according to (9), luminosity compensation according to (16).

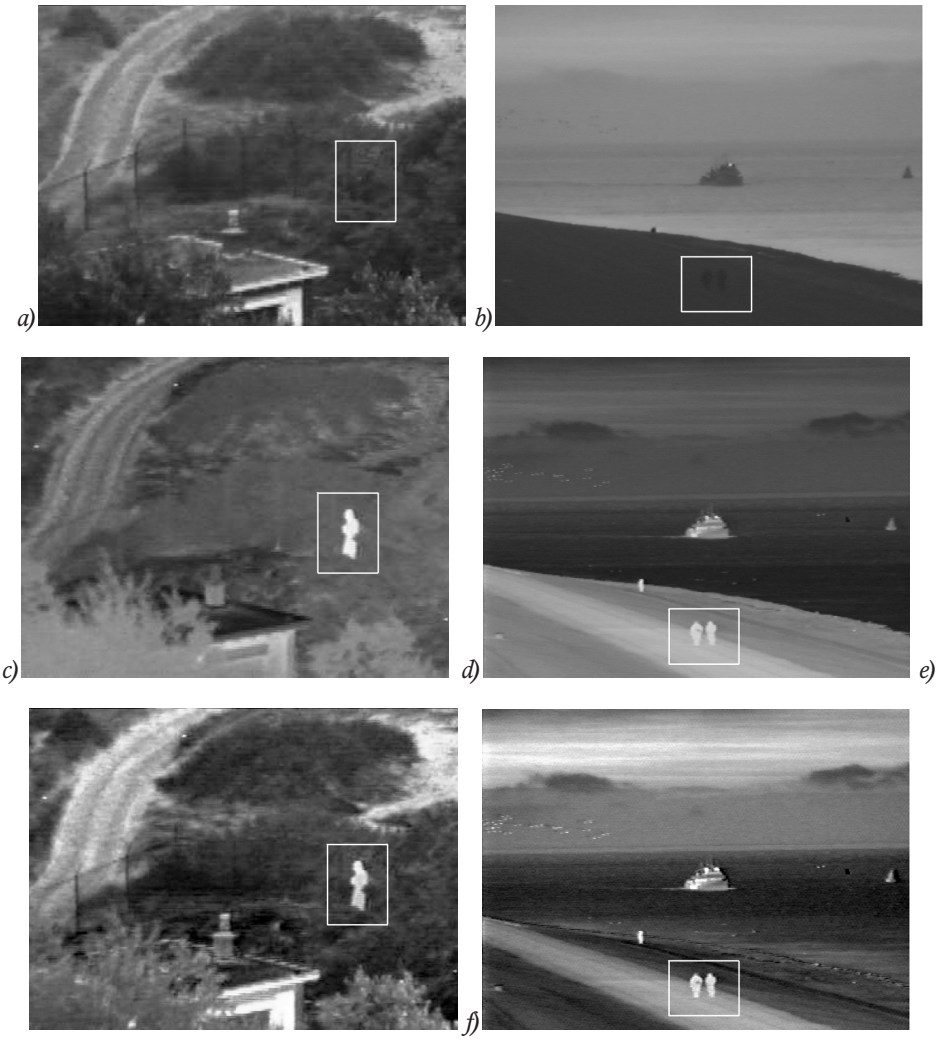

Fig. 4. Resulting TV and TI fusion images (grayscale)

The resulting grayscale fusion images according to (2) followed by histogram reduction are shown in Fig. 4*e*, *f*. Color fusion was performed for the benchmark parameter vector $\mathbf{V}_t = ||\text{-}10, \text{-}12, 20, 35||^{\mathrm{T}}$ [35]. According to Vorobel' method, a local contrast was evaluated for each frame (Table 2):

$$K_{\mathrm{v}} = |\ \overline{Y}_{\mathrm{s}} - \overline{Y}_{\mathrm{b}}\ | / Y_{\max},$$

where $\overline{\ }$ and $\overline{Y}_{\mathrm{b}}$ are the average brightness of the subject and background, respectively (evaluation area of the background brightness is marked by a white rectangle in Fig. 4*a*-*f*), and $Y_{\max}$ is the greatest pixel brightness in the image.

Table 2. Local contrast K_{v}

Picture	4*a*	4*b*	4*c*	4*d*	4*e*	4*f*
$K_{\mathrm{в}}$	0.02	0.03	0.54	0.10	0.70	0.16

The comparative results of color-based image fusion algorithms are given in cloud computing services [38]. Since functional transformations with TV and TI images performed in algorithms 1–3 are homogeneous [39], a parallel computing technology, such as CUDA, may be used to improve the method performance [40, 41]. The results for NVIDIA GeForce GTS450 Graphics Card (32 cores were invoked for the parallel computing) are given in Table 3.

It follows from the obtained results that the simplified color-transfer-based image fusion algorithm (algorithm 3) and the resulting color images provide the method performance 1.12 times greater than algorithm 2 proposed in paper [36]. In this case, evaluations of standard deviations of the C_b and C_r components according to (13) and (14) differ at most by a factor of 0.3 %.

Table 3. Performance of color-transfer-based image fusion algorithms for TV and TI images with the resulting color images, frames per second (fps)

Algorithm	1	2	3
On CPU	2.8	4.9	5.5
On GPU with CUDA	19.1	33.5	37.8

The Gaussian hypothesis on distribution of chromatic multicolor components C_b and C_r, with simplified computation according to (13), was tested using the Chi-Square Test for false-color fusion images obtained from TV and TI frames in Fig. 4*a* and *c*, respectively. Since, according to (13), the values of C_{bf} and C_{rf} are equal in their absolute magnitudes, only distribution of component C_b has been analyzed (Fig. 5). It also follows from (13) that $-128 \le C_b \le 128$, therefore for computational convenience we have selected a number of decomposition intervals of equal width $k = 16$ (the given value for the frame size of 1024×768 is less than the recommended number of intervals $k_{\mathrm{st}} = 20$ being obtained by Sturges formula [42]:

$k_{\mathrm{st}} = 3.3\lg(n) + 1$,

where n is a number of sample elements).

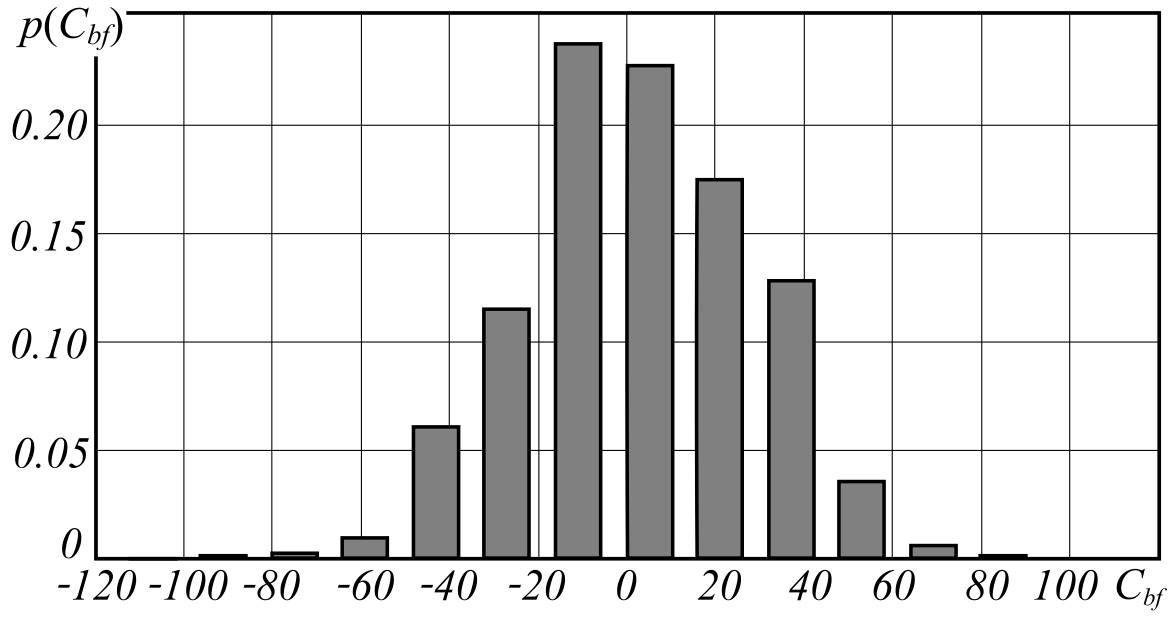

Fig. 5. Distribution histogram for C_b

For significance level $\alpha = 0.05$, the critical value $\chi^2 = 7.539 < \chi^2_{(\alpha,\, k-3)} = 22.362$ is calculated using the Chi-Square method, therefore the Gaussian hypothesis for C_b and C_r is being confirmed.

Conclusion

Thus, the simplified algorithm considered in this paper implements real-time grayscale image fusion in TV and TI sensors (with aligned images for increased fields of view) providing the same luminosity of the resulting gray fusion and color fusion images.

References

1. Kostyaskin LN, Babaev SI, Loginov AA, Pavlov OV. Technology of Improved. Synthesized Vision Systems to Aircraft Control. Proc of Technical Vision in the Control Systems of Mobile Objects: 2010 Mar 16-18; Tarusa, 2010.

2. Zheng Y, Essock EA, Hansen BC. An Advanced Image Fusion Algorithm Based on Wavelet Transform – Incorporation with PCA and Morphological Processing. Proc SPIE 2004; 5298: 177-187.

3. Das S, Krebs WK. Sensor Fusion of Multi-spectral Imagery. Institution of Electrical Engineers: Electronics Letters 2000; 36: 1115-1116.

4. Wang W, Chang F. A Multi-focus Image Fusion Method Based on Laplacian Pyramid. Journal of Computers 2011; 6(12): 2559-2566.

5. Anshakov GP, Raschupkin AV, Zhuravel YN. Hyperspectral and Multispectral Resurs-P Data Fusion for Increase of Their Informational Content. Computer Optics 2015; 39(1): 77-82.

6. Zheng Y, ed. Image Fusion and Its Applications. Rijeka: InTech; 2011.

7. Toet A, Hogervorst MA. Progress in Color Night Vision. Optical Engineering 2012; 51(1): 1-19.

8. Shi S, Wang L, Jin W, Zhao Y. Color Night Vision Based on Color Transfer in YUV Color Space. Proc SPIE 2008; 6623: 66230B.

9. Bogdanov AP, Kholopov IS. Algorithms of Color Fusion from Monochrome Multispectral Images Based on Color Conversion Methods [In Russian]. Digital Signal Processing 2013; 3: 26-32.

10. Christinal JJ, Jebaseeli TJ. A Novel Color Image Fusion for Multi Sensor Night Vision Images. International Journal of Computer Applications Technology and Research 2013; 2(2): 155-159.

11. Brown LG. A Survey of Image Registration Techniques. ACM Computing Surveys 1992; 24(4): 325-376.

12. Parker JA, Kenyon RV, Troxel DE. Comparison of Interpolating Methods for Image Resampling. IEEE Trans on Medical Imaging 1983; MI-2(1): 31-39.

13. Lu F, Zhuangzhi W, Xiang L. Fast Image Diffusion for Feature Detection and Description. International Journal of Computer Theory and Engineering 2015; 8(1): 58-62.

14. Heather JP, Smith MI. Multimodal Image Registration with Applications to Image Fusion. Proc of 7th IEEE International Conference on Information Fusion 2005, Jul 25-28.

15. Hui L, Manjunath BS, Mitra SK. A Contour-Based Approach to Multisensor Image Registration. IEEE Trans on Image Processing 1995; 4(3): 320-334.

16. Oliveira FPM, Tavares JMRS. Matching Contours in Images Using Curvature Information and Optimization Based on Dynamic Programming. IEEE Latin America Trans 2009; 7(6): 703-712.

17. Muratov ER, Nikiforov MB. Methods of Reducing the Computational Complexity of Combining Disparate Images [In Russian]. Cloud of Science 2014; 1(2): 327-336.

18. Bhosle U, Roy SD, Chaudhuri S. Multispectral Panoramic Mosaicing. Pattern Recognition Letters 2005; 26(4): 471-482.

19. Hines GD, Rahman Z, Jobson DJ, Woodell GA. Multi-Image Registration for an Enhanced Vision System. Proc SPIE 2003; 5108: 231-241.

20. Zhang Z. A Flexible New Technique for Camera Calibration. IEEE Transactions on Pattern Analysis and Machine Intelligence 2000; 22(11): 1330-1334.

21. Tsai RY. A Versatile Camera Calibration Technique for High-Accuracy 3D Machine Vision Metrology Using Off-The-Shelf TV Cameras and Lenses. IEEE Journal on Robotics and Automation 1987; 3(4): 323-344.

22. Kovalenko VP, Veselov YuG, Karpikov IV. The Method of Distortion Estimation for Modern Infrared Systems [In Russian]. Vestnik MSTU of NE Bauman 2011; 1: 98-107.

23. Goshin YeV, Fursov VA. 3D Scene Reconstruction from Stereo Images with Unknown Extrinsic Parameters. Computer Optics 2015; 39(5): 770-776.

24. Muratov ER. The Construction of the Virtual Terrain Model Using Stereo Vision System [In Russian]. Proc of Technical Vision in Control Systems Conference, 2015, Mar 17-19. Moscow: ISR RAS; 2015.

25. Hartley R, Zisserman A. Multiple View Geometry in Computer Vision. Cambridge: Cambridge University Press; 2003.

26. Bogdanov AP, Romanov VYu, Romanov YuN. Visible and Infrared Image Fusion [In Russian]. Proceedings of the of the 11th Conference on Problems Transmission and Processing of Information in Networks and Telecommunications Systems, 2002, Mar 28-29. Ryazan; 2002.

27. Drynkin VN, Falkov EYa, Tsareva TI. The Forming of the Composite Image in the Zonal Airborne Aerospace System [In Russian]. Proc Of Technical Vision in Control Systems Conference, 2012, Mar 14-16. Moscow: ISR RAS; 2012.

28. Gonzalez RC, Woods RE. Digital Image Processing. Digital Signal Processing. 2nd edition. London: Pearson Education Ltd; 2001.

29. Vizilter YuV, Zheltov SYu, Bondarenko AV, Ososkov MV, Morzhin AV. Image Processing and Analysis Tasks in Machine Vision: Lectures and workshops [In Russian]. Moscow: "Fizmatkniga" Publisher; 2010.

30. Lloyd JM. Thermal Imaging Systems. NY: Springer Science + Business Media, LLC; 1975.

31. Usamentiaga R, Venegas P, Guerediaga J, Vega L, Molleda J, Bulnes FG. Infrared Thermography for Temperature Measurement and Non-Destructive Testing. Sensors 2014; 14: 12305-12348.

32. Tarasov VV, Torshina IP, Yakushenkov YuG. 3rd Generation Infrared Systems [In Russian]. Moscow: "Logos" Publisher; 2011.

33. Reinhard E, Ashikhmin M, Gooch B, Shirley P. Color Transfer between Images. IEEE Computer Graphics and Applications 2001; 21: 34-41.

34. Bogdanov AP, Pavlov OV, Kholopov IS. Improve the Performance of Algorithms for Form a Color Fusion Image from Multispectral Monochrome Sensors Signals [In Russian]. Digital Signal Processing 2013; 3: 33-37.

35. Bogdanov AP, Pavlov OV, Kholopov IS. False Color Fusion Algorithms and Color Accent in the Problems of Combining Information from the Monochrome Multispectral Sensors of Vision Systems [In Russian]. Technical Vision 2014; 2: 49-54.

36. Li G, Xu S, Zhao X. Fast Color-Transfer-Based Image Fusion Method for Merging Infrared and Visible Images. Proc SPIE 2010; 7710: 77100S.

37. Kholopov IS. Detection of Signals in Radar Systems with the Adaptive Chaotic Pulse Clutters Recognition Algorithm [In Russian]. Vestnik RGRTU 2011; 36: 33-8.

38. Color Fusion Results: Pictures for the Paper. Source: https://disk.rsreu.ru/public.php?service=files&t=182057bc2d34bdb1e788b7bcb4094063.

39. Gruzman IS, Kirichuk VS, Kosykh VP, Peretyagin GI, Spektor AA. Digital Image Processing in Information systems [In Russian]. Novosibirsk: NSTU Publisher; 2002.

40. Vizilter YuV, Gorbatsevich VS, Rubis AYu, Vygolov OV. Image Shape Matching Using Diffusion Morphology and Diffusion Correlation. Computer Optics 2015; 39(2): 265-274.

41. Sanders J, Kandrot E. CUDA by Example. NY: Addison-Wesley; 2010.

42. Lemeshko BYu, Chimitova EV. On the choice of the number of intervals in the criteria for the consent of chi-square test [In Russian]. Industrial laboratory. Materials diagnostics 2003; 69: 61-67.